# Engineering interfacial molecular interactions on Ag Hollow fibre gas diffusion electrodes for high efficiency in CO<sub>2</sub> conversion to CO

Yizhu Kuang <sup>a</sup>, Guoliang Chen <sup>a</sup>, Dimuthu Herath Mudiyanselage <sup>b</sup>, Hesamoddin Rabiee <sup>a,c,d\*</sup>, Beibei Ma <sup>c</sup>, Fatereh Dorosti <sup>c</sup>, Ashok Kumar Nanjundan <sup>a,b</sup>, Zhonghua Zhu <sup>c</sup>, Hao Wang <sup>a,b,\*</sup>, Lei Ge <sup>a,b,\*</sup>

- <sup>a.</sup> Centre for Future Materials, University of Southern Queensland, Springfield, QLD 4300, Australia. E-mail: <u>lei.ge@usq.edu.au</u>, <u>hao.wang@usq.edu.au</u>
- b. School of Engineering, University of Southern Queensland, Springfield, QLD 4300, Australia
- <sup>c.</sup> School of Chemical Engineering, The University of Queensland, Brisbane, QLD 4072, Australia.
- University of Bern, Department of Chemistry, Biochemistry and Pharmaceutical Sciences, Freiestrasse 3, 3012 Bern, Switzerland. E-mail: hesamoddin.rabiee@unibe.ch

#### Abstract

The electrochemical CO<sub>2</sub> reduction reaction (CO<sub>2</sub>RR) occurs at the nanoscale interface of the electrode-electrolyte. Therefore, tailoring the interfacial properties in the interface microenvironment provides a powerful strategy to optimise the activity and selectivity of electrocatalysts towards the desired products. Here, the microenvironment at the electrodeelectrolyte interface of the flow-through Ag-based hollow fibre gas diffusion electrode (Ag HFGDE) is modulated by introducing surfactant cetyltrimethylammonium bromide (CTAB) as the electrolyte additive. The porous hollow fibre configuration and gas penetration mode facilitate the CO<sub>2</sub> mass transfer and the formation of the triple-phase interface. Through the ordered arrangement of hydrophobic long-alkyl chains, CTAB molecules at the electrode/electrolyte interface promoted CO<sub>2</sub> penetration to active sites and repelled water to reduce the activity of competitive hydrogen evolution reaction (HER). By applying CTABcontaining catholyte, Ag HFGDE achieved a high CO Faradaic efficiency (FE) of over 95 % in a wide potential range and double the partial current density of CO. The enhancement of CO selectivity and suppression of hydrogen was attributed to the improvement of charge transfer and the CO<sub>2</sub>/H<sub>2</sub>O ratio enhancement. These findings highlight the importance of adjusting the local microenvironment to enhance the reaction kinetics and product selectivity in the electrochemical CO<sub>2</sub> reduction reaction CO<sub>2</sub>RR.

#### Introduction

Electrochemical CO<sub>2</sub> reduction reaction (CO<sub>2</sub>RR) is a promising approach to upgrade CO<sub>2</sub>, as a primary greenhouse gas, into valuable fuels and chemical feedstocks driven by renewable energy, facilitating the path towards carbon neutrality [1]. The CO<sub>2</sub>RR process starts with CO<sub>2</sub> molecules being adsorbed onto vacant sites on the electrocatalyst surface, and subsequently, multiple protons and electrons are transferred to generate intermediates and products [2]. Nonetheless, the low solubility of CO<sub>2</sub> molecules in the bulk of aqueous electrolytes and the sluggish mass transfer have limited the efficiency of CO<sub>2</sub> conversion <sup>[3]</sup>. Recently, gas-diffusion electrodes (GDEs) have been implemented to boost mass transport by providing adequate CO2 supply and strengthening the triple-phase interface reaction among the gaseous phase, electrocatalyst and electrolyte [4]. GDEs can directly deliver CO<sub>2</sub> in the neighbourhood of the electrocatalyst, achieving optimal CO<sub>2</sub> concentration and minimising the diffusion distance. Traditional planar GDEs composed of multiple layers frequently suffer from a high hydrogen evolution reaction (HER) owing to the flow-by gas diffusion pathway, in which the electrocatalytic reaction relies on the concentration of dissolved CO<sub>2</sub> in the aqueous electrolyte [5]. This results in favourable conditions for hydrogen gas production. Hollow fibre flowthrough GDEs or gas-penetration electrodes (GPEs) are more advanced GDE structures for CO2RR because of the facilitated mass transfer, abundant electrocatalytic active sites, and reduced cell complexities [6]. The distinctive features of hollow fibre GDEs (HFGDEs) effectively enhanced the kinetics of CO<sub>2</sub>RR, exhibiting significant promise in gas-phase electrolysis such as CO<sub>2</sub>RR <sup>[7]</sup> or CORR <sup>[8]</sup>. For instance, fabricating silver-based hollow fibre GDEs (Ag HFGDEs) has been promising in converting CO<sub>2</sub> into CO, coupled with a high reaction rate and conversion in the CO<sub>2</sub>RR <sup>[9]</sup>. However, eliminating the competitive reaction of HER in pristine HFGDEs is still challenging, considering the wetting of outer surfaces in contact with electrolytes and water trapping in small hydrophilic pores. Surface electrocatalyst engineering strategies on HFGDE, such as nanostructuring, re-structuring and heterogenous atom doping, have successfully enhanced product selectivity [9-10].

Besides the intrinsic activity of electrocatalysts, the microenvironment at the electrodeelectrolyte interface during the electrocatalytic reaction also plays a crucial role in the CO<sub>2</sub>RR process <sup>[11]</sup>. Recent studies indicated that surface modification at the electrode and electrolyte interface with solvated alkali metal ions <sup>[12]</sup>, polymers <sup>[13]</sup>, charged organic surfactants <sup>[14]</sup>, etc., could effectively modulate the interfacial environment, particularly charge distribution and hydrophobicity. For example, sodium dodecyl sulfate (SDS) is an anionic surfactant that brings about different surface charges, which in turn affects the dispersion and morphology characteristics of electrocatalytic particles [15]. Non-ionic surfactants, polyvinylpyrrolidone (PVP), can be used as capping agents in nanomaterials synthesis, stabilising the structure, maintaining the defined morphology, avoiding particle agglomeration, and mitigating irregular growth [16]. In addition, refining the electrolyte composition by adding a surfactant into the electrolyte, could efficiently regulate the ion distribution and adjust the CO<sub>2</sub>/H<sub>2</sub>O ratio, thereby improving mass transfer at the electrode/electrolyte interface in the electrocatalytic CO2 conversion process. Employing surfactant dodecylphosphonic acid (DDPA) and its analogues as electrolyte additives could modulate the interfacial H-bond environment on Ag NPs electrode [17]. This work showed that the surfactant additive increased the CO<sub>2</sub>RR activity towards CO while suppressing the kinetics of the HER, resulting from promoting the hydrogenation of CO<sub>2</sub> to \*COOH evidenced by the in situ infrared spectroscopy. Moreover, the surfactant molecule of cetyltrimethylammonium bromide (CTAB), comprised of a polar headgroup and hydrophobic long-chain groups, has been proven to enhance the charge transfer and adjust the local CO<sub>2</sub>/H<sub>2</sub>O ratio in CO<sub>2</sub>RR. Under an external potential, the CTAB molecules could be adsorbed on the electrode surface, forming a dense layer with a hierarchal structure through charge interactions. The ordered CTAB assembly in the electrode/electrolyte interface could improve the charge transfer and regulate the interfacial water by reducing protons close to the compact layer's outer Helmholtz plane (OHP). This resulted in forming a hydrophobic microenvironment, reducing the local proton source for the side reaction of HER and improving the CO<sub>2</sub>/H<sub>2</sub>O ratio in reaction active areas in CO<sub>2</sub> conversion [18]. For instance, an interfacial microenvironment containing cationic surfactants CTAB on commercial Ag electrodes could effectively improve the electrocatalytic performance in selectivity and reaction activity of CO<sub>2</sub> conversion to CO [18a]. Owing to forming an ordered surfactant assembly at the electrode-electrolyte interface, the surfactant CTAB in electrolyte facilitated the distribution of interfacial CO<sub>2</sub> and H<sub>2</sub>O, which promoted the charge transfer to CO formation. Meanwhile, repelling the isolated water molecules into order structure formed a hydrophobic microenvironment, thereby inhibiting the HER [18a]. Besides, the density functional theory (DFT) calculation revealed that the modification of CTAB in the electrode/electrolyte interface could remarkably decrease the energy barrier of CO\* desorption, which benefited the reaction activity and product selectivity in CO<sub>2</sub> conversion into CO <sup>[19]</sup>.

Herein, we exploited the structural advantages of Ag hollow fibre GDEs (Ag HFGDEs) combined with modulating the microenvironment of the electrode-electrolyte interface with

CTAB to suppress the HER and achieve improved CO conversion. The concentration effects of CTAB on HER suppression and charge transfer have been investigated. The result demonstrated that, after introducing surfactant CTAB into catholyte, the Ag HFGDE can operate in a wide potential range at high current densities to convert CO<sub>2</sub> to CO. Furthermore, the advantage of HFGDE configuration has been presented by significantly improved reaction activity and selectivity for CO when the AgHF electrode operated in a GDE configuration compared to the non-GDE configuration within the same CTAB-containing catholyte systems.

#### **Experimental section**

### Preparation of pristine silver hollow fibres

Silver hollow fibres (AgHF) were prepared by a phase-inversion and thermal treatment process as in our previous works <sup>[9]</sup>. Briefly, the silver powder (99.9% purity, 1 um, Shanghai Xiangtian Nano Materials Co., China) was added to the solvent of N-methyl-2-pyrrolidone (NMP, Sigma-Aldrich Co., Australia). Then, the polymer binder of polyethersulfone (PES, Ultrason E 6020 P, BASF, Germany) was added to obtain a homogeneous slurry in a ball milling. The slurry was extruded through a spinneret rig and shaped into a microtubular in the water bath (18.2  $M\Omega \cdot cm$ ) via a phase-inversion process. The formed tubes were left in the water overnight to ensure complete removal of the solvent. The PES polymer binder was removed in the calcination process using a tubular furnace in the air atmosphere (600 °C for 6 h). the shiny silver metallic lustre AgHF tubes, named pristine AgHF, were obtained.

#### **Characterisation of materials**

The surface and cross-section morphologies of AgHF samples were studied via a JOEL-7100F scanning electron microscopy (SEM). FTIR spectra were measured on a Perkin Elmer Spectrum 100. Crystalline structures of the bulk of AgHF samples were examined through X-ray diffraction (XRD) utilising a Bruker device with a Cu K $\alpha$  ( $\lambda$  =1.5418Å) radiation source. X-ray photoelectron spectroscopy (XPS) measurements were carried out using a Kratos Axis ULTRA XPS, which included a hemispherical electron energy analyser (165 nm) and a monochromatic Al K $\alpha$  (1486.6 eV) radiation source, operating at 15 kV (10 mA). XPS data was analysed using the CASA® software, calibrated against the C1s signal at 284.4 eV.

#### Electrochemical reduction of CO<sub>2</sub> and product analysis

All electrochemical experiments were carried out in a three-electrode H-type electrochemical cell with Ag hollow fibres (Ag HF) as the working electrode and gas delivery at room

temperature. The length of Ag HF was around 3 cm measured by a digital vernier calliper. The Ag HF was sealed with epoxy at one end, and the other end was connected to the gas inlet of the cell. The effective area was calculated via the formulation of  $S=\pi D_{out}L$ . where  $D_{out}$  refers to the outer diameter of Ag HF, and L is the exposed length of Ag HF. For each test, the actual reaction area was measured. The anode chamber and cathode chamber were separated by a Nafion-117 proton exchange membrane. Ag/AgCl electrode (in a 3.0 M NaCl Luggin capillary) and Pt mesh were used as reference and counter electrodes, respectively. The electrolyte was 0.5 M KHCO<sub>3</sub> with additives of different concentrations of surfactant cetyltrimethylammonium bromide (CTAB). The electrolyte without CTAB was designated as 0 mM CTAB, while those with CTAB were labelled as 0.2 mM CTAB, 0.5 mM CTAB, and 0.8 mM CTAB, corresponding to the surfactant concentration in the electrolyte. The Nernst equation was applied to convert the potentials from the Ag/AgCl scale to the RHE reference scale: E(V vs. RHE) = E(V vs.Ag/AgCl) +  $E^0$  (Ag/AgCl) + 0.0591pH. A potentiostat controlled the electrochemical reaction potential and collected data, including Cyclic voltammetry (CV), Linear sweep voltammetry (LSV), electrochemical impedance spectroscopy (EIS), and Chronoamperometry. Prior to the experiment, the electrolyte underwent CO<sub>2</sub> gas purging for at least 30 minutes. CO<sub>2</sub> was continuously fed through the hollow fibre to the catholyte at a 20 ml/min flow rate throughout the electrolysis process. The flow rate was regulated and monitored by the MFC 2100 Series mass flow controller. A potential sweep from -0.7 to -2 V vs. Ag/AgCl was applied in the LSV at a scan rate of 5 mV/s.

To assess the active surface area of AgHF, the double-layer capacitance ( $C_{dl}$ ) determined from CV scans was conducted over a 0.1 V window near the open-circuit potential at scan rates from 20 to 120 mV s<sup>-1</sup>. The following equation can be used to calculate the  $C_{dl}$  from CV:

$$C_{dl} = j/(\frac{dV}{dt})$$

Where C represents the capacitance, j is the current density at the centre of 0.1 V potential window, and  $\frac{dV}{dt}$  refers to the CV scan rate.

The electrochemical impedance spectroscopy (EIS) was measured at various potentials from 100 kHz to 0.1 Hz. The Nyquist plots were fitted using an equivalent circuit to simulate the experimental data. The double-layer capacitance ( $C_{dl}$ ) from EIS was calculated using the equation below:

$$C_{dl} = \left\{ R_{ct}^{(1-n)} CPE \right\}^{(1/n)}$$

Where  $R_{ct}$  is the charge transfer resistance, CPE is the constant phase element, and n is the fitting parameter. The Zview2 software was employed to fit the relevant parameter values.

To determine the faradaic efficiency (FE) at various potentials, chronoamperometry was conducted for 25 minutes at potential ranging from -0.8 to -1.5 V vs. RHE. A gas chromatograph (GC, Shimadzu 2014) was employed to detect gas products (mainly H<sub>2</sub> and CO) quantitatively. The FE can be computed through the equation provided below:

$$FE_i(\%) = \frac{e_i \times F \times V \times P \times X_i}{J \times R \times T} \times 100$$

Where  $e_i$  represents the number of electron transfers per mole of gas product, F is known as the Faradaic constant, V presents the gas flow rate, P refers to the atmospheric pressure,  $X_i$  stands for the product concentration, J presents the total current acquired from the potentiostat, R represents the ideal gas constant, and T refers to the temperature.

#### **Results and Discussions**

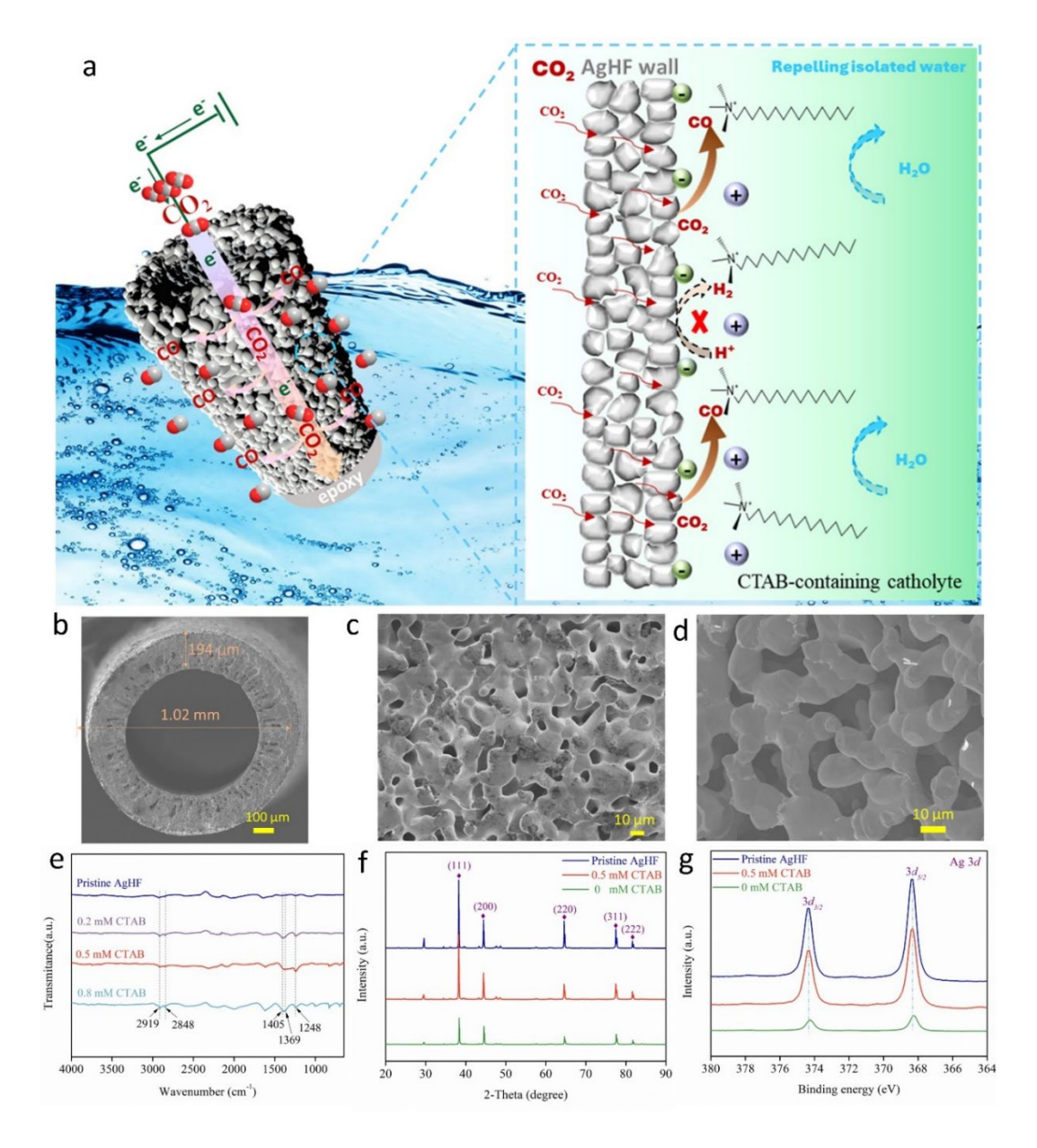


Figure 1. (a) schematic illustration showing the processes of CO<sub>2</sub> conversion over Ag HFGDE. SEM images of (b) cross-section, (c) outer and (d) inner surfaces of pristine Ag HFGDE. (e) The FTIR spectra of pristine Ag HFGDE and Ag HFGDE after CO<sub>2</sub>RR testing in different concentrations of CTAB-containing catholytes. (f) XRD patterns, (g) XPS spectra of Ag 3d over pristine Ag HFGDE and Ag HFGDE after CO<sub>2</sub>RR testing in the catholyte with/without CTAB.

The schematic of the silver hollow fibre (AgHF) electrode (**Figure 1a**) illustrates the hierarchical micro/nanostructures composed exclusively of metallic silver, which acted as a CO<sub>2</sub> diffuser through the porous framework of the walls and current collector as well as the active sites for CO<sub>2</sub>RR. The porous structure of Ag HFGDEs effectively increases the active sites, facilitating CO<sub>2</sub> mass transport to the electrocatalyst-electrolyte interface. The cross-

section SEM image in Figure 1b showed that the AgHF has a homogeneous morphology with a wall thickness of 194 µm and outer diameter of 1.0 mm. The AgHF surface featured numerous micro-sized and interconnected pores on the outer and inner surfaces (Figure 1c and 1d), facilitating CO<sub>2</sub> penetration and ensuring a sufficient gas supply in the electrochemical reaction [20]. The FTIR data for the pristine Ag HFGDE and the Ag HFGDE after testing in different concentrations of CTAB-containing catholyte are illustrated in Figure 1e. In the FTIR spectrums, the appearance of new groups in all CTAB-containing systems compared with pristine Ag HFGDE was observed. As can be seen in Figure 1e, peaks at 2919 and 2848 cm<sup>-1</sup> were attributed to the C-H stretching vibration of the -CH<sub>2</sub> group in CTAB <sup>[21]</sup>. The peaks at 1405 and 1369 cm<sup>-1</sup> were caused by the C-H bending vibration, while the band of 1248 cm<sup>-1</sup> could be assigned to the C-N stretching vibration [21-22]. The crystal structure of Ag HFGDEs before and after testing in CTAB-containing catholyte was evaluated by XRD patterns (Figure 1f and Figure S1). The defined diffraction peaks at 2-Theta values of 38.2°, 44.4°,64.7°,77.6°, and 91.8° corresponding to the (111), (200), (220), (311), and (222) planes of the face-centred cubic structure of silver, respectively [18b]. This indicated that the adsorption of CTAB on the surface of the electrocatalyst did not alter the crystalline structure of the AgHF. The intensity of AgHF in CTAB-containing catholyte was remarkably stronger compared with CTAB-free catholyte, which was argued to exhibit higher activity towards CO<sub>2</sub> conversion [9, 18a]. Moreover, XPS spectra of Ag HFGDEs after testing in CTAB-containing catholyte observed strong metallic Ag characteristic peaks at 368.4 eV and 374.4 eV, corresponding to Ag 3d<sub>5/2</sub> and Ag 3d<sub>3/2</sub> peaks, respectively, identical to those observed in the pristine AgHF (Figure 1g and Figure S2).

# Electrocatalytic performance of CO<sub>2</sub>RR

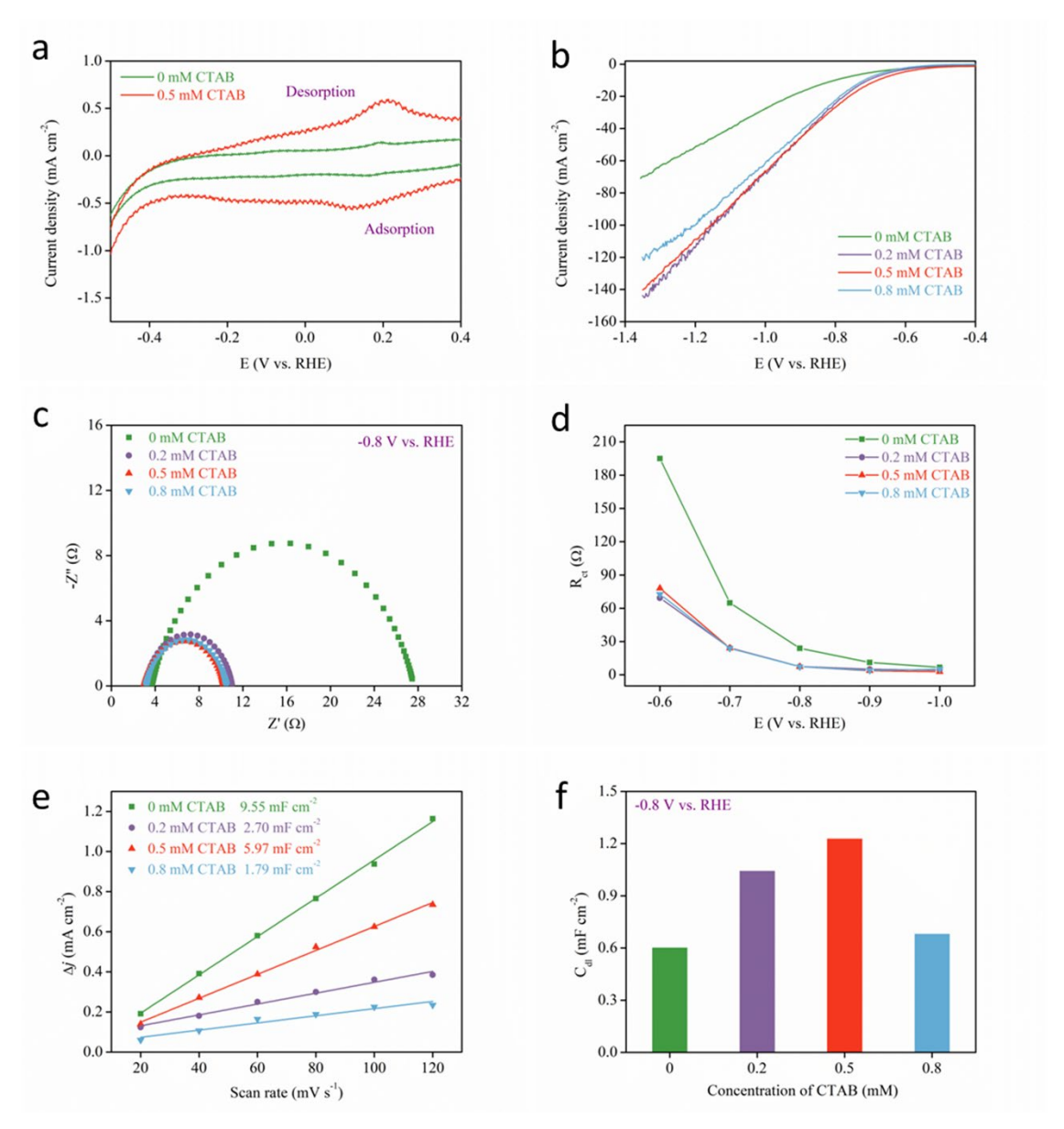


Figure 2. (a) cyclic voltammogram curves for multiple scans in CTAB-containing/free catholyte (0.5mM and 0 mM, respectively) at a scan rate of 0.05 V s<sup>-1</sup>. (b) Linear sweep voltammetry of Ag HFGDEs in electrolytes containing different concentrations of CTAB. (c) Nyquist plots of Ag HFGDEs in CTAB-containing/free catholyte at -0.8 V vs. RHE. (d) Charge transfer resistances of Ag HFGDEs in CTAB-containing/free catholyte. (e) Plot of Δ*j* against the scan rates of cyclic voltammogram. (f) The interfacial electrochemical double-layer capacitance of Ag HFGDEs obtained from EIS with an equivalent circuit in CTAB-containing/free catholyte.

The electrocatalytic CO<sub>2</sub>RR performance in CTAB-containing/free catholyte was systematically investigated in a two-chamber H-shaped electrolyser with a three-electrode system. The 0.5 M KHCO<sub>3</sub> solution electrolyte containing different concentrations of CTAB

(0 mM, 0.2 mM, 0.5 mM, and 0.8 mM) was employed. As shown in Figure 2a, a distinctive reversible adsorption/desorption peak in the cyclic voltammogram (CV) was observed in the 0.5 mM CTAB-containing catholyte (0.5 mM CTAB system), which was not presented in the CTAB-free catholyte (0 mM CTAB system). This could be associated with the pseudocapacitance features resulting from the reversible adsorption and desorption of surfactant CTAB [23]. Similar pseudocapacitance features were recorded in different CTAB concentrations, as shown in Figure S3. To evaluate the reaction activity of Ag HFGDEs in different electrolyte systems, linear sweep voltammetry (LSV) was applied. As depicted in Figure 2b, corresponding trends in all systems featured lower current densities at less negative potential and an increase as overpotentials increased. Compared to the CTAB-free catholyte, the Ag HFGDEs in the CTAB-containing catholyte exhibited higher current densities at a potential period from -0.65 to -1.35 V vs. RHE. As an illustration, the current densities of AgHF significantly escalated to 140.1 mA cm<sup>-2</sup> at -1.35 V vs. RHE in the 0.5 mM CTAB system, whereas it was merely 70.9 mA cm<sup>-2</sup> in the CTAB-free system. The doubling of current density in CTAB-containing catholyte implied that introducing CTAB molecules created a favourable interfacial microenvironment that enhanced ion diffusion and charge transfer during the CO<sub>2</sub> conversion process, resulting in an enhancement in the reactivity of the CO<sub>2</sub>RR. Nonetheless, it was worth noting that the current densities have a slight decline in the 0.8 mM CTABcontaining catholyte (0.8 mM CTAB system) in comparison with 0.2 mM and 0.5 mM CTABcontaining catholyte (0.2 mM CTAB system and 0.5 mM CTAB system, respectively) at -1.35 V vs. RHE. This could be ascribed to the saturation of CTAB in electrolytes, which diminished its contribution to the activity of CO<sub>2</sub> conversion <sup>[24]</sup>.

To further explore the interfacial behaviour in CTAB-containing catholytes and their charge transfer and mass transfer characteristics on the surface of Ag HFGDEs, electrochemical impedance spectroscopy (EIS) was probed at relevant electrocatalytic testing conditions. Nyquist plots in electrolytes containing different concentrations of CTAB were displayed in **Figure 2c** at -0.8 V vs. RHE. Compared to the CTAB-free catholyte, the Ag HFGDE under CTAB-containing catholytes indicated lower interfacial charge transfer resistance ( $R_{ct}$ ). A lower  $R_{ct}$  reflected the decrease of the activation energy barrier for the electron transfer in the formation of \*COO- intermediate and fastened initial electron transfer step, which could effectively improve CO<sub>2</sub> conversion with high activity and selectivity [25]. The value of  $R_{ct}$  in different potentials under different CTAB-containing catholytes was explored in **Figure 2d**. The result indicated that the values of  $R_{ct}$  in CTAB-containing catholytes were lower than those

of CTAB-free catholytes in all testing potentials. The reduction in charge transfer resistance observed in the CTAB-containing catholyte was attributed to the ordered distribution of adsorbed CTAB molecules on the electrode surface. These CTAB molecules organized and structured the interface between the electrode and the electrolyte, which enhanced ion diffusion towards the electrode and facilitated the efficiency of charge transfer across the electrode-electrolyte interface [18a].

The electric double-layer capacitance  $(C_{dl})$  gained from scanning CV at different scan rates represented the reaction active sites at the electrocatalyst surface. As shown in Figure 2e and Figure S4, the values of Cdl from CV in CTAB-containing catholytes were 2.70 mF cm<sup>-2</sup> for  $0.2~\mathrm{mM}$  CTAB system,  $5.97~\mathrm{mF}$  cm<sup>-2</sup> for  $0.5~\mathrm{mM}$  CTAB system, and  $1.79~\mathrm{mF}$  cm<sup>-2</sup> for  $0.8~\mathrm{mM}$ CTAB system, respectively, which were much lower than that in the CTAB-free catholyte (9.55 mF cm<sup>-2</sup>). The reduction of  $C_{dl}$  (gained from the CV) in CTAB-containing catholyte could likely be attributed to the adsorption of CTAB molecules on the Ag electrocatalyst surface, which occupied part of reactive active sites. On the other hand, the interfacial electrochemical double-layer capacitance ( $C_{dl}$ ) obtained from EIS using an equivalent circuit (**Figure S5**) reflected the charge accumulation at the electrode-electrolyte interface [26]. Specifically, the capacitance will increase if more mobile ions are present in the bulk electrolyte. As illustrated in Figure 2f, the Ag HFGDEs in the CTAB-containing catholyte showed a higher interfacial charge capacitance than those in the CTAB-free catholyte. For example, the capacitance was 1.23 mF cm<sup>-2</sup> in the 0.5 mM CTAB system, doubling the value observed in the 0 mM CTAB system (0.60 mF cm<sup>-2</sup>). The results demonstrated that the existing surfactant of CTAB in electrolytes provided more mobile ions to be adsorbed on the Ag HFGDE surface. This also provided evidence from the decrease of charge transfer resistance observed in the CTABcontaining system in Figure 2d. Furthermore, compared with the other two in CTABcontaining catholyte, the 0.5 mM CTAB system showed a higher catalytic active surface area and interfacial charge capacitance, which was expected to achieve enhanced CO2RR performance.

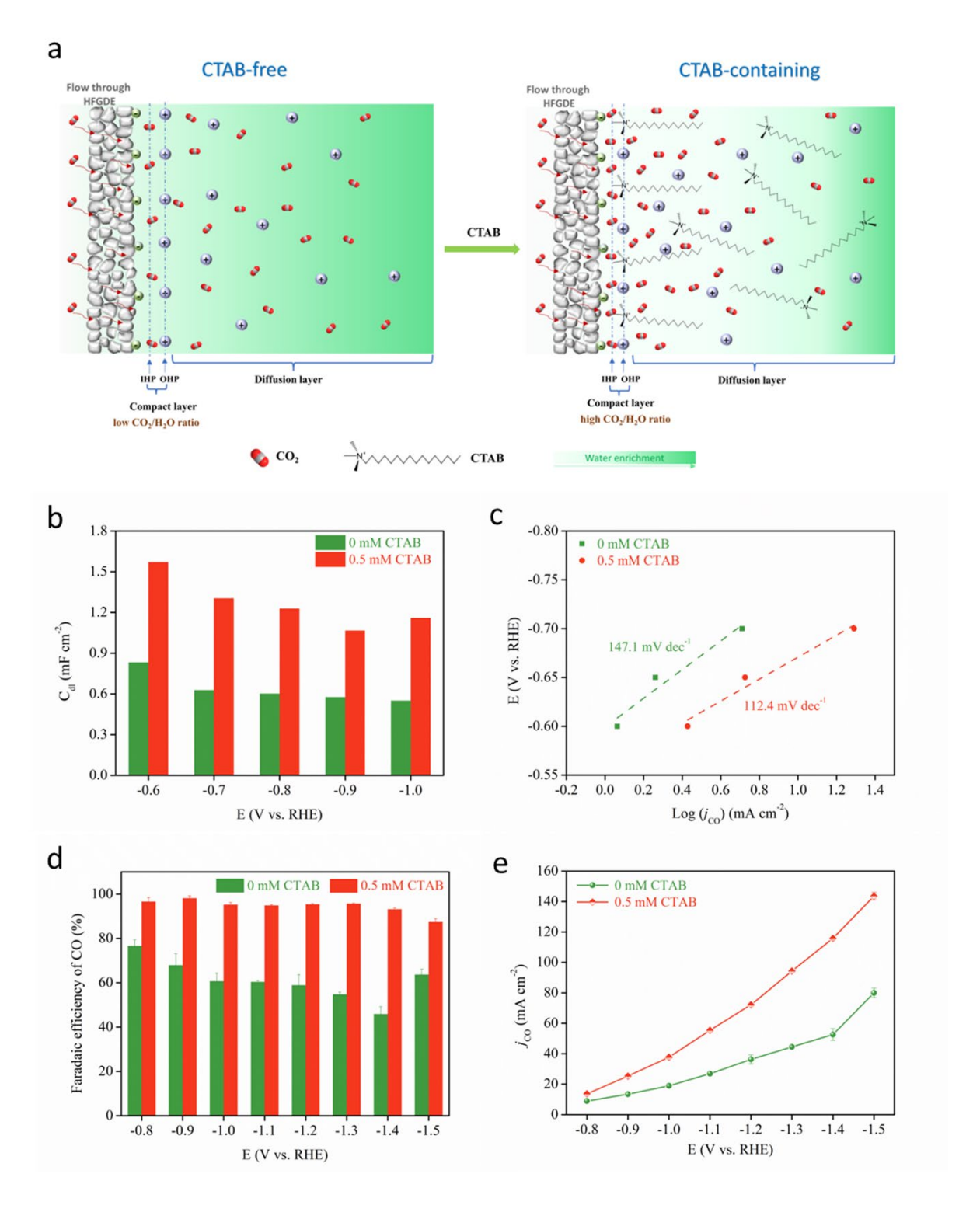


**Figure 3. (a)** Schematic of electrochemical double-layer on the flow through HFGDE surface before and after adding CTAB into the electrolyte. **(b)** The interfacial double-layer capacitance obtained from EIS at different potentials in 0.5 mM CTAB and 0 mM CTAB systems. **(c)** Tafel plots of Ag HFGDE in 0.5 mM CTAB and 0 mM CTAB systems. **(d)** Faradaic efficiency of

CO at -0.8 to -1.5 V vs. RHE for Ag HFGDE in 0.5 mM CTAB and 0 mM CTAB systems, and (e) their corresponding CO partial current densities.

It is known that applying a potential on an electrode in the electrolyte generates an electrochemical double layer (EDL) in which oppositely charged solvated molecules accumulate to neutralise the charge at the electrode interface [27]. The EDL at the interface can be separated into a compact layer and a diffusion layer, in which the compact layer is the primary site of the potential drop in the current electrolyte system (**Figure 3a**). The compact layer can be further divided into inner Helmholtz planes (IHP) and outer Helmholtz planes (OHP). As schematically shown in **Figure 3a**, the CTAB molecules in CTAB-containing catholyte could form an ordered structure on the Ag HFGDE surface and lead to tighter Helmholtz layers at the compact layer, which can effectively facilitate the charge transfer at the interface and improve the CO<sub>2</sub>/H<sub>2</sub>O ratio [26]. Therefore, the interfacial double-layer capacitance (*Cdl*) obtained from EIS at different potentials in 0.5 mM CTAB and 0 mM CTAB systems were further examined in **Figure 3b**. The value of C<sub>dl</sub> in the 0.5 mM CTAB system was higher than that of the CTAB-free system at applied potentials. These EIS experiments demonstrated the strengthened capacity of CTAB to regulate the local ion concentration and facilitate the charge transfer at the Ag HFGDE surface.

The analysis of Tafel plots provided insight into the kinetic mechanism for CO<sub>2</sub>RR in CTAB-containing/free catholyte (**Figure 3c** and **Figure S6**). Tafel slopes in the CTAB-containing catholyte were lower than the absent CTAB system, indicating that the absorbed CTAB molecules on the AgHF surface boosted the reaction kinetics of CO<sub>2</sub> conversion into CO <sup>[28]</sup>. In detail, the reaction for the electroreduction of CO<sub>2</sub> to CO production over an Ag-based electrocatalyst occurs in the following steps:<sup>[29]</sup>

$$CO_2 + e^- \rightarrow COO^{*-} \tag{1}$$

$$COO^{*-} + H^+ \rightarrow COOH^* \tag{2}$$

$$COOH^* + H^+ + e^- \rightarrow CO^* + H_2O$$
 (3)

$$CO^* \to CO + ^* \tag{4}$$

In the above reaction process, the initial step was one-electron transfers to CO<sub>2</sub> to form adsorbed COO\*- (step 1), followed by the formation of COOH\* intermediate through protonation of COO\*- (step 2). Then, a proton-electron transfer and dehydration occurred to form a CO\* intermediate (step 3), and finally, the formed CO\* was desorbed from the silver

surface to gain CO production. The step 1 was believed to be the rate-determining step owing to its high energy barrier required [30]. The Tafel slope was 112.4 mV dec<sup>-1</sup> in the 0.5 mM CTAB system, 127.4 mV dec<sup>-1</sup> in the 0.2 mM CTAB system and 136.6 mV dec<sup>-1</sup> in the 0.8 mM CTAB system, respectively, which was lower than that of in 0 Mm CTAB system (147.1 mV dec<sup>-1</sup>), as shown in **Figure 3c** and **Figure S6**. These results demonstrated that the added surfactant CTAB into catholyte could enhance the intrinsic catalytic activity of AgHF towards CO formation. The Tafel slope of 112.4 mV dec<sup>-1</sup> in 0.5 mM CTAB system was very close to the theoretical value of 118 mV dec<sup>-1</sup>, indicating a more rapid initial electron transfer to the CO<sub>2</sub> molecule for the formation of COO\* intermediate (step 1). This phenomenon was also consistent with the lower interfacial charge transfer resistance (*Rct*) on the Ag HFGDE in the 0.5 mM CTAB system (**Figure 2c**). These observations verified the enhancement of electron transfer and the intrinsic CO<sub>2</sub> reduction activity by introducing CTAB into the catholyte.

The effects of CTAB-containing catholyte on the product selectivity and reaction activity of Ag HFGDEs were further explored by chronopotentiometry at various potentials, as shown in Figures 3d and 3e. CO and H2 were the primary products of CO2RR for all catholyte systems, and their combined Faradic efficiency (FE) was close to 100% (Figures S7 and S8). As illustrated in Figure 3d, an outstanding performance of the Ag HFGDE in the 0.5 mM CTAB system was observed in a wide potential window of -0.8 to -1.5 V vs. RHE. The FE of CO exceeded 95% within the potential range of -0.8 V to -1.3 vs. RHE, with a slight decrease observed at -1.4 and -1.5 V vs. RHE. In detail, the FE of CO could reach a maximum value of 98.15% with a partial current density ( $j_{co}$ ) of 25.0 mA cm<sup>-2</sup> at -0.9 V vs. RHE after introducing CTAB into catholyte, while the FE of CO was 67.90% with j<sub>co</sub> of 13.4 mA cm<sup>-2</sup> in CTAB-free catholyte. Even at a highly negative potential of -1.5 V vs. RHE, the FE of CO remained ~90% with  $j_{co}$  of 143.6 mA cm<sup>-2</sup>. This was ascribed to the fact that the CTAB could modulate the CO<sub>2</sub>/H<sub>2</sub>O ratio at the electrode and electrolyte interface and facilitate the charge transfer on the double-layer microenvironment. As discussed in Figure 3a, the long chain of CTAB molecules forms an ordered structure, leading to a tighter Helmholtz layer at the compact layer, thereby promoting interfacial charge transfer. The EIS experiments also demonstrated the improved ability of CTAB to reduce the  $R_{ct}$  and increase the interfacial  $C_{dl}$  at the Ag HFGDE surface. Besides, the long alky chain in CTAB molecules could effectively adjust the water environment at the electrified interface by repelling isolated water to form a highly hydrophobic interfacial microenvironment, which improved the CO<sub>2</sub>/H<sub>2</sub>O ratio at the electrode and electrolyte interface [18a]. Furthermore, the presence of CTAB in the catholyte could prevent the hydrogen atoms

from interfacial water molecules moving towards the electrode surface, which led to an increased Ag-H distance and reduced water dissociation activity [18a, 31]. As a result, the competitive reaction of HER in the Ag HFGDE was effectively inhibited, while the CO<sub>2</sub> conversion was promoted in CTAB-containing catholyte. Furthermore, the CO<sub>2</sub>RR stability was evaluated in 0.5 mM CTAB-containing catholyte at -1.1 V vs. RHE. The FE of CO remained over 90% with a partial current of over 50 mA cm<sup>-2</sup> (**Figure S9**), indicating that the enhanced electrode/electrolyte interface can effectively benefit the FE of CO and reaction activity with stable operation in CTAB-containing catholyte.

# The pathway of CO<sub>2</sub> distribution in Ag HFGDEs

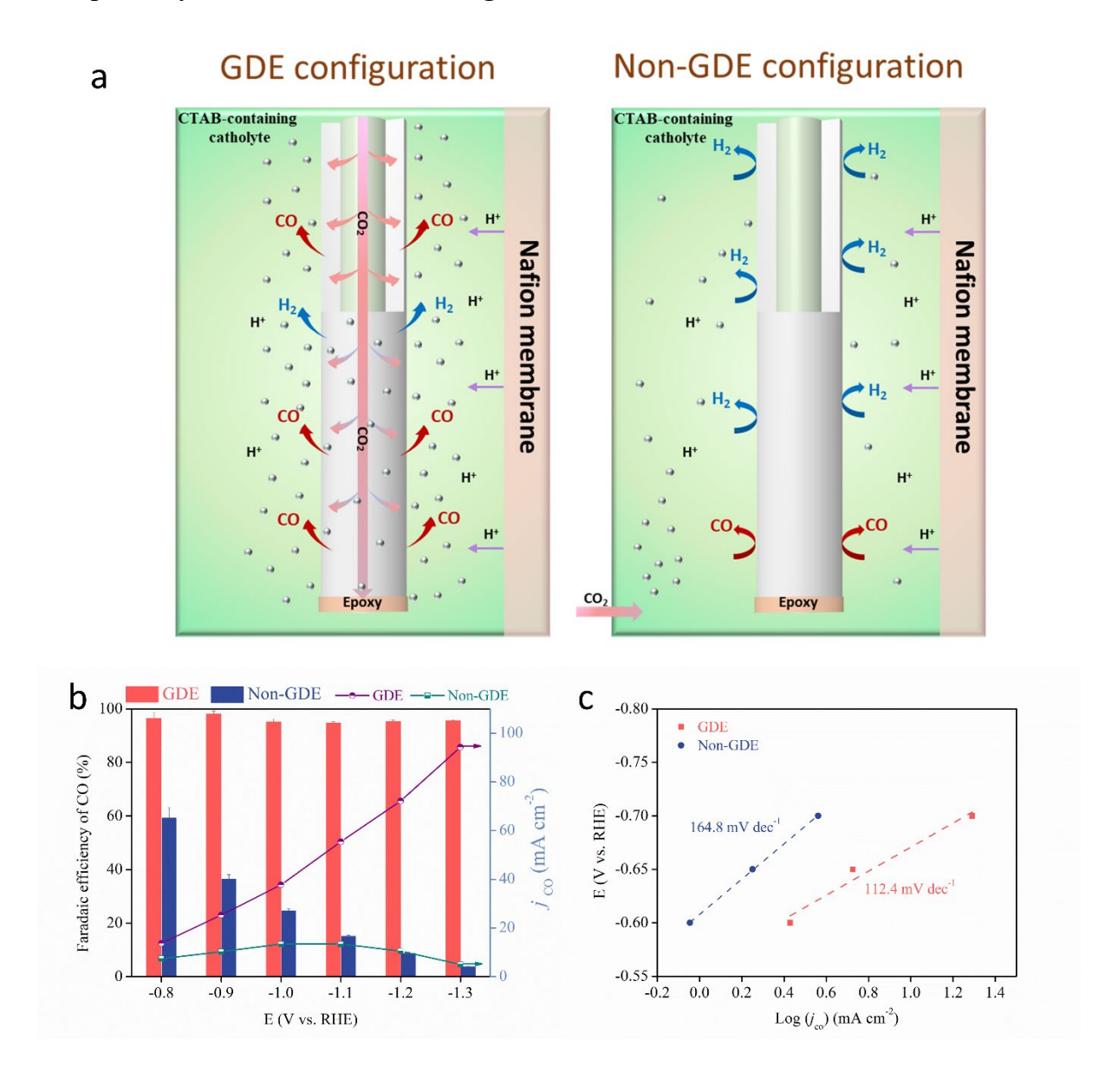


**Figure 4. (a)** Schematic of CO<sub>2</sub> delivery pathways in GDE and non-GDE configuration; **(b)** Faradaic efficiency of CO in the range of -0.8 to -1.3 V vs. RHE on AgHF electrode in CTAB-

containing catholyte in both GDE and non-GDE configurations and their corresponding partial current densities ( $j_{co}$ ). (c) Tafel slopes of AgHF electrode in GDE and Non-GDE configurations.

Compared to planar Ag electrodes in a similar electrolyte reported in the literature, the Ag HFGDE presented a considerably higher electrocatalytic activity for CO<sub>2</sub> conversion into CO. It was reported that the highest partial current density of CO in CTAB-containing systems was 30.6 mA cm<sup>-2</sup> with a 96.0% FE for Ag foil and 29.8 mA cm<sup>-2</sup> with an 82.2% FE for Ag NPs, respectively, at -1.2 V vs. RHE [18a]. The reason was the low solubility and diffusion of CO<sub>2</sub> in flat Ag electrodes within aqueous electrolytes. The Ag HFGDE achieved a CO partial current density of 72.2 mA cm<sup>-2</sup> with an FE of 96.0% at the same potential in the CTAB-containing system. This was attributed to the unique gas diffusion pathway in the AgHF electrode. The Ag HFGDE penetrated CO<sub>2</sub> via a flow-through mechanism, as illustrated in Figure 4a. One side of the Ag HFGDE was sealed by epoxy, while the gas was fed from the other side and penetrated through the porous AgHF walls by pressure differential. This flow-through gaseous feed effectively supplied sufficient CO2 to the active electrocatalyst surface, creating a high local CO<sub>2</sub> concentration near the triple-phase interface sites, which was essential for achieving high current density in CO<sub>2</sub> conversion <sup>[32]</sup>. To further validate the advantage of CO<sub>2</sub> delivery in Ag HFGDE for enhancing the electrocatalytic activity of CO<sub>2</sub> conversion, we examined the AgHF electrode in a non-GDE configuration under the same CTAB-containing catholyte for electrocatalytic CO<sub>2</sub> reduction. As shown in Figure 4a, the CO<sub>2</sub> gas outlet was placed directly into the electrolyte, allowing the CO<sub>2</sub> to be dissolved within the electrolyte. The FE of CO was significantly reduced in the non-GDE configuration compared to the GDE configuration, as displayed in Figure 4b. Meanwhile, the partial current density of CO in the non-GDE configuration (jco: 5.0 mA cm<sup>-2</sup>) was nearly 19 times lower than that in the GDE configuration (jco: 94.3 mA cm<sup>-2</sup>) at -1.3 V vs. RHE, confirming that numerous available electrocatalytic active sites were not utilised in non-GDE configuration. Besides, penetrating CO2 through the hollow fibre in the GDE configuration could facilitate the desorption and removal of the CO product from the reaction sites and prevent the blockage of electrocatalytic active sites, which effectively improved the reaction activity of CO<sub>2</sub> reduction <sup>[33]</sup>. Furthermore, Tafel slopes were evaluated to explore the kinetic behaviour of CO<sub>2</sub>RR in GDE and non-GDE configurations. In Figure 4c, the Tafel slope of the AgHF electrode in the non-GDE configuration was 164.8 mV dec<sup>-1</sup>, whereas it was 112.4 mV dec<sup>-1</sup> in the GDE configuration. A higher Tafel slope observed in the non-GDE configuration implied that the GDE configuration supplied more excellent electrocatalytic activity and more efficient CO<sub>2</sub> mass transport to the active sites.

#### Conclusion

In summary, we illustrated that the interfacial modification of Ag HFGDE via introducing surfactant CTAB into electrolytes can boost reaction activity and selectivity of CO<sub>2</sub> conversion into CO. The results indicated that the CTAB additive facilitated the charge transfer in the interfacial and reduced the local water concentration to suppress the competing reaction of HER. The Ag HFGDE in CTAB-containing catholyte achieved a high FE of over 95% in a wide potential range, and the partial current density of CO exhibited two times higher than in CTAB-free catholyte. Moreover, the structural features of hollow fibre GDE greatly enhanced the CO<sub>2</sub> mass transfer and optimised the formation of the triple-phase interface, leading to CO<sub>2</sub> conversion with superior activity and selectivity towards CO production. Our study provides a straightforward and efficient approach for regulating the interfacial properties of reaction electrode-electrolyte surfaces to enhance the CO<sub>2</sub>RR performance, which can be applied to diverse electrocatalytic gas conversion reactions.

# Acknowledgements

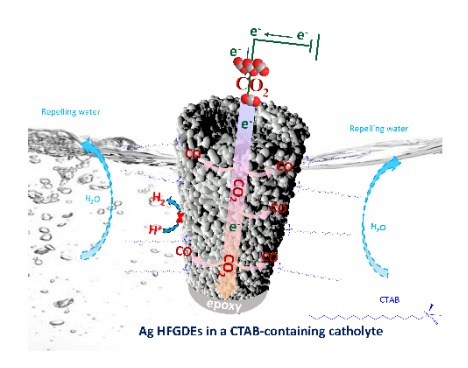
We acknowledge financial support from the ARC Future Fellowship (FT220100166), Discovery project (DP190101782) and Centre of Excellence for Green Electrochemical Transformation of Carbon Dioxide (CE230100017).

**Keywords**: electrochemical CO<sub>2</sub> reduction reaction, surfactant CTAB, charge transfer, microenvironment, electrode/electrolyte interface

- [1] a) J. Zhang, J. Ding, Y. Liu, C. Su, H. Yang, Y. Huang, B. Liu, *Joule* 2023, 7, 1700-1744; b) W. Lai, Y. Qiao, Y. Wang, H. Huang, *Adv. Mater.* 2023, 35, 2306288; c) D. Segets, C. Andronescu, U. P. Apfel, *Nat. Commun.* 2023, 14, 7950; d) M. Chen, K. Chang, Y. Zhang, Z. Zhang, Y. Dong, X. Qiu, H. Jiang, Y. Zhu, J. Zhu, *Angew. Chem. Int. Ed.* 2023, 62, e202305530.
- [2] Y. Kuang, H. Rabiee, L. Ge, T. E. Rufford, Z. Yuan, J. Bell, H. Wang, *Energy Environ. Mater.* **2023**, *6*, e12596.
- [3] a) S. Lu, Y. Wang, H. Xiang, H. Lei, B. B. Xu, L. Xing, E. H. Yu, T. X. Liu, *J. Energy Storage* **2022**, *52*, 104764; b) M. Alfath, C. W. Lee, *Catalysts* **2020**, *10*, 859.
- [4] a) H. Rabiee, L. Ge, X. Zhang, S. Hu, M. Li, Z. Yuan, Energy Environ. Sci. 2021, 14, 1959-2008; b) H. Rabiee, M. Li, P. Yan, Y. Wu, X. Zhang, F. Dorosti, X. Zhang, B. Ma, S. Hu, H. Wang, Z. Zhu, L. Ge, Adv. Sci. 2024, 11, 2402964.
- [5] B. Endrodi, E. Kecsenovity, A. Samu, F. Darvas, R. Jones, V. Torok, A. Danyi, C. Janáky, *ACS energy lett.* **2019**, *4*, 1770-1777.
- [6] a) H. Rabiee, L. Ge, J. Zhao, X. Zhang, M. Li, S. Hu, S. Smart, T. E. Rufford, Z. Zhu, H. Wang, Appl. Catal. B Environ. 2022, 310, 121362; b) H. Rabiee, L. Ge, S. Hu, H. Wang, Z. Yuan, Chem.Eng. J. 2022, 450, 138476-138496; c) Y. Gao, X. Tu, X. Liu, Y. Zhang, M. Huang, J. Zhu, H. Jiang, ChemCatChem 2024, 16, e202400361.
- [7] a) H. Rabiee, L. Ge, X. Zhang, S. Hu, M. Li, S. Smart, Z. Zhu, Z. Yuan, Appl. Catal. B 2021, 286, 119945-119956; b) H. Rabiee, X. Zhang, L. Ge, S. Hu, M. Li, S. Smart, Z. Zhu, Z. Yuan, ACS Appl. Mater. Interfaces 2020, 12, 21670-21681.

- [8] H. Rabiee, J. K. Heffernan, L. Ge, X. Zhang, P. Yan, E. Marcellin, S. Hu, Z. Zhu, H. Wang, Z. Yuan, *Appl. Catal. B Environ.* **2023**, *330*, 122589-122598.
- [9] Y. Kuang, G. Chen, H. Rabiee, B. Ma, F. Dorosti, A. K. Nanjundan, Z. Zhu, H. Wang, L. Ge, *Energy Fuels* **2024**, 38, 10096-10105.
- [10] a) H. M. Jeong, Y. Kwon, J. H. Won, Y. Lum, M. J. Cheng, K. H. Kim, M. Head-Gordon, J. K. Kang, Adv. Energy Mater. 2020, 10, 1903423; b) Y. J. Liu, P. Shao, M. Y. Gao, W. H. Fang, J. Zhang, Inorg. Chem. 2020, 59, 11442-11448; c) G. Chen, L. Ge, Y. Kuang, H. Rabiee, B. Ma, F. Dorosti, A. K. Nanjundan, Z. Zhu, H. Wang, Small Sci. 2024, 4, 2400184; d) G. Chen, L. Ge, Y. Kuang, H. Rabiee, B. Ma, F. Dorosti, A. K. Nanjundan, Z. Zhu, H. Wang, Chem. Eng. J. 2024, 490, 151651.
- [11] a) P. Yue, Q. Fu, J. Li, L. Zhang, D. Ye, X. Zhu, Q. Liao, ACS Appl. Mater. Interfaces 2023, 15, 53429-53435; b) M. Zeng, W. Fang, Y. Chen, X. Zhang, Y. Hu, B. Y. Xia, Angew. Chem. 2024, 136, e202404574; c) H. Wu, A. Singh-Morgan, K. Qi, Z. Zeng, V. Mougel, D. Voiry, ACS Catal. 2023, 13, 5375-5396.
- [12] J. Resasco, L. D. Chen, E. Clark, C. Tsai, C. Hahn, T. F. Jaramillo, K. Chan, A. T. Bell, *J. Am. Chem. Soc.* **2017**, *139*, 11277-11287.
- [13] S. Ahn, K. Klyukin, R. J. Wakeham, J. A. Rudd, A. R. Lewis, S. Alexander, F. Carla, V. Alexandrov, E. Andreoli, *ACS Catal.* **2018**, *8*, 4132-4142.
- [14] Y. Zhong, Y. Xu, J. Ma, C. Wang, S. Sheng, C. Cheng, M. Li, L. Han, L. Zhou, Z. Cai, *Angew. Chem.* **2020**, *132*, 19257-19263.
- [15] L. Shi, Y. Zhang, X. Han, D. Niu, J. Sun, J. Y. Yang, S. Hu, X. Zhang, Chin. J. Chem. 2019, 37, 337-341.
- [16] a) R. Reske, H. Mistry, F. Behafarid, B. Roldan Cuenya, P. Strasser, J. Am. Chem. Soc. 2014, 136, 6978-6986; b) M. P. L. Kang, H. Ma, R. Ganganahalli, B. S. Yeo, ACS Catal. 2023, 14, 116-123.
- [17] X. Yuan, W. Ge, Y. Zhu, L. Dong, H. Jiang, C. Li, ACS Appl. Mater. Interfaces 2024, 16, 38083-38091.
- [18] a) W. Ge, Y. Chen, Y. Fan, Y. Zhu, H. Liu, L. Song, Z. Liu, C. Lian, H. Jiang, C. Li, J. Am. Chem. Soc. 2022, 144, 6613-6622; b) W. Wang, S. Gong, H. Wang, Y. Tan, X. Zhu, X. Wang, J. Liu, W. Yu, G. Zhu, X. Lv, Chem. Eng. J. 2024, 490, 151849.
- [19] H. Pan, F. Wang, Z. Zhang, S. Min, Sustain. Energy Fuels **2022**, *6*, 2149-2154.
- [20] H. Rabiee, L. Ge, X. Zhang, S. Hu, M. Li, S. Smart, Z. Zhu, H. Wang, Z. Yuan, *Appl. Catal. B Environ.* **2021**, *298*, 120538.
- [21] Z. Q. Zhang, S. Banerjee, V. S. Thoi, A. Shoji Hall, J. Phys. Chem. Lett. 2020, 11, 5457-5463.
- [22] G. Su, C. Yang, J. J. Zhu, Langmuir 2015, 31, 817-823.
- [23] C. D. Xu, J. Y. Ye, L. Chen, D. H. Chen, J. T. Li, C. H. Zhen, S. G. Sun, *Electrochim. Acta* 2015, 162, 129-137.
- [24] S. Banerjee, C. S. Gerke, V. S. Thoi, Acc. Chem. Res. 2022, 55, 504-515.
- [25] S. Li, X. Dong, Y. Zhao, J. Mao, W. Chen, A. Chen, Y. Song, G. Li, Z. Jiang, W. Wei, *Angew. Chem.* **2022**, *134*, e202210432.
- [26] S. Sarkar, A. Maitra, S. Banerjee, V. S. Thoi, J. M. Dawlaty, J. Phys. Chem. B 2020, 124, 1311-1321.
- [27] J. Wu, Chem. Rev. 2022, 122, 10821-10859.
- [28] a) J. Rosen, G. S. Hutchings, Q. Lu, S. Rivera, Y. Zhou, D. G. Vlachos, F. Jiao, ACS Catal. 2015, 5, 4293-4299; b) A. Thevenon, A. Rosas-Hernández, A. M. Fontani Herreros, T. Agapie, J. C. Peters, ACS Catal. 2021, 11, 4530-4537.
- [29] S. A. Mahyoub, F. A. Qaraah, C. Chen, F. Zhang, S. Yan, Z. Cheng, *Sustain. Energy Fuels* **2020**, *4*, 50-67.
- [30] D. D. Zhu, J. L. Liu, S. Z. Qiao, *Adv. Mater.* **2016**, *28*, 3423-3452.
- [31] C. Y. Li, J. B. Le, Y. H. Wang, S. Chen, Z. L. Yang, J. F. Li, J. Cheng, Z. Q. Tian, *Nat. Mater.* **2019**, *18*, 697-701.
- [32] M. Duarte, B. De Mot, J. Hereijgers, T. Breugelmans, ChemElectroChem 2019, 6, 5596-5602.
- [33] H. Rabiee, J. K. Heffernan, L. Ge, X. Zhang, P. Yan, E. Marcellin, S. Hu, Z. Zhu, H. Wang, Z. Yuan, *Appl. Catal. B Environ.* **2023**, *330*, 122589.

# **Graphical abstract**



The silver hollow fibre gas diffusion electrode (Ag HFGDE) acts as a  $CO_2$  diffuser through the porous wall, effectively converting  $CO_2$  to CO while suppressing the HER in a CTAB-containing catholyte.